Chapter 3

Quantum chemistry calculations

This chapter deals with the quantum chemical results. After a description of the computational details, CASSCF geometry optimizations (section 3.2) and CASPT2 and TD-DFT vertical excitation energies (section 3.3) are presented and compared with MR-CCI results (section 3.4). Next, the calculated MR-CCI potential energy curves and transition dipole moments are shown in section 3.5. Then the kinetic coupling terms are calculated using the MR-CCI wave functions (section 3.6). Finally, section 3.7 investigates the ionic states potentials and approximate transition dipole moments.

3.1 Computational details

For the sake of simplicity, all the calculations described in this work have been done assuming C_S symmetry and a staggered configuration, as depicted in figure 1.7 of the Introduction (section 1.2.2).

3.1.1 Basis sets

Effective core potential basis sets (ECPs) make use of the fact that in a chemical sense a large number of core electrons are unimportant and only the valence electrons participate in the chemical reactions. The inner electrons can, therefore, be described by pseudopotentials or effective core potentials. Relativistic effects, which are most important for core electrons of heavy atoms of the lower half of the periodic table, can be treated by these potentials. ECPs exist also for second row elements, even though the saving of computational time is small relative to all-electron calculations. $CpMn(CO)_3$ has 102 electrons. In this work the ten inner electrons of manganese and the two core electrons of the carbon and the oxygen atoms are described in the relativistic effective core potential approximation ECP (small core). The contraction schemes for the remaining electrons, effective atomic number Z=15.0 for manganese, Z=6.0 for oxygen and Z=4.0 for carbon are as follows: A (8s,7p,6d,1f) set contracted to [6s,5p,3d,1f] (Z=15.0) for the Mn atom [109], for the oxygen atoms a (4s,5p) set contracted to [2s,3p] (Z=6.0) [110] and for the carbon atoms a (4s,4p) set contracted to [2s,2p] (Z=4.0) [110].

An Atomic Natural Orbital (ANO) basis set was used for the hydrogen atom. Natural orbitals, typically from a correlated CISD calculation, are used for a contraction of a large number of primitive Gauss Type Orbitals (GTOs) to a small number of contracted GTOs. For a restricted Hartree Fock wave function the ANOs would be the same as the canonical orbitals with occupation numbers of either 0 or 2. When a correlated wave function is used the occupation number can be any number between 0 and 2. The magnitude of the occupation number governs the choice of the primitive GTOs used in the contractions. In this work the ANO basis set (7s,3p) contracted to [3s,1p] was applied for the H atoms [111].

The multiconfigurational calculations have been carried out with the MOLCAS-4 Quantum Chemistry software [112][1] and the TD-DFT with GAUSSIAN-98 series of programs [113].

3.1.2 Applied *ab initio* methods

The a^1A' electronic ground state configuration of CpMn(CO)$_3$ conforms to a closed shell occupation

$$(20a')^2(21a')^2(22a')^2(12a'')^2(13a'')^2$$

corresponding to the

$$(2\pi_{Cp})^2(3d_{z^2})^2(3d_{x^2-y^2})^2(3\pi_{Cp})^2(3d_{xy})^2$$

electronic configuration. Low-lying virtual orbitals correspond to $3d_{yz}(23a')$, $3d_{xz}(14a'')$ and $\pi^*_{CO}(24a'$, $25a'$, $15a''$ and $16a'')$.

CASSCF wavefunctions were used in subsequent MS-CASPT2 calculations in order to calculate the vertical excitation spectrum (section 3.3). This method is *the state of the art* for achieving chemical accuracy in the calculation of excitation energies. However, for the given basis set and active space, the CASSCF wavefunction was not a good reference for a MS-CASPT2 treatment of dissociation. The method of choice in such problematic cases is the MR-CCI treatment based on CASSCF reference wave functions. In both the MS-CASPT2 and the MR-CCI description the previous CASSCF calculations were averaged over several roots of a given spin and symmetry. In the active space ten electrons were correlated

---

[1] The author is grateful to Roland Lindh for providing a preliminary version of the MS-CASPT2 software

in fourteen orbitals including the highest π_{Cp} occupied orbitals, the $3d_{Mn}$ occupied and vacant orbitals, the $3d$ of correlation and the low-lying π^*_{CO} orbitals. This active space, so-called 10e14a, constitutes a good starting point for the addition of dynamical correlation effects by means of the CASPT2 treatment in the multi-state approach (with a level shift correction of 0.5 E_h). An active space limited to 10 electrons correlated in 10 active orbitals (the previous 10e14a space without the four low-lying π^*_{CO} orbitals) has also been used for the purpose of CASSCF geometry optimizations in order to study the effect of the quality of the CASSCF wavefunction on the calculated bond lengths and angles. Transition dipole moments were estimated at the CASSCF level.

Vertical excitation energies and transition dipole moments have also been studied using TD-DFT and the same basis set employed in the CASSCF computations (described in section 3.1.1). In particular, two different functionals were used, namely the B3LYP and the local approach BP86. The exchange functional B3 is the hybrid method proposed by Becke [114] that includes a mixture of Slater functional [115], Becke's 1988 gradient correction [116] and Hartree-Fock exchange. Its correlation part, LYP, is the gradient corrected functional of Lee, Yang and Parr [117]. In the BP86 functional, the exchange-correlation potential corresponds to the gradient approximated potential (GGAs) by Becke [118] for the exchange and Perdew [119] for correlation.

The ground state CASSCF optimized geometry with the large CASSCF 10e14a active space has been used in the calculation of the Franck-Condon energies (MS-CASPT2, TD-DFT and MR-CCI) and transition dipole moments (CASSCF, MR-CCI) and for the calculation of the potential energy curves along the stretching coordinate of the Mn-CO$_{ax}$ bond (MR-CCI).

3.2 CASSCF and DFT geometry optimizations

The geometry optimizations have been performed under the C$_S$ symmetry constraint which is a reasonable assumption as discussed in section 1.2.2. Starting from the gas phase staggered geometry (figure 1.7 (a)) CASSCF optimizations have been performed for the a^1A' electronic ground state and a few low lying singlet A' excited states in order to follow the geometry changes that take place when exciting the molecule. The geometries of η_5-CpMn(CO)$_3$ and η_5-CpMn(CO)$_2$ have been also optimized at the DFT (B3LYP) level of theory.

3.2.1 Structure of the parent molecule η^5-CpMn(CO)$_3$

The CASSCF optimized geometries of η_5-CpMn(CO)$_3$ in its electronic ground state a^1A' and in the three low-lying excited states b^1A', c^1A' and d^1A' corresponding to $3d_{Mn} \rightarrow 3d_{Mn}$ excitations (see section 3.3) are reported in table 3.1. The optimized ground state geometry is compared to the DFT (B3LYP) geometry and to the experimental structures in gas-phase and solid state.

Bond lengths^a	Gas-phase^b	Solid state^c	a^1A' DFT	$a^1A'^d$	b^1A'	$c^1A'^e$	d^1A'
Mn-C$_{ip}$	1.808	1.780, 1.797	1.793	1.810 (1.830)	1.994 (1.996)	2.846 (2.249)	1.919 (1.966)
Mn-C$_{op}$	1.808	1.780, 1.797	1.794	1.806 (1.831)	1.977 (1.997)	1.883 (1.904)	1.960 (1.967)
Mn-C$_{ring}$ ^{f}	2.149	2.124, 2.151	2.203	2.231 (2.215)	2.361 (2.335)	2.245 (2.328)	2.404 (2.370)
C-O ^{a}	1.148	1.150, 1.134	1.173	1.148 (1.146)	1.138 (1.138)	1.135 (1.136)	1.141 (1.139)
C-C ^{a}	1.424	1.388, 1.394	1.434	1.420 (1.420)	1.418 (1.416)	1.422 (1.415)	1.421 (1.417)
Bond Angles							
C$_{ip}$-Mn-C$_{ip}$	91.9	92.0	94.0	93.2 (93.6)	94.7 (93.4)	85.4 (91.5)	102.7 (100.4)
C$_{op}$-Mn-C$_{op}$	91.9	92.0	93.4	92.5 (92.9)	95.0 (93.0)	106.5 (102.2)	94.0 (91.9)

Table 3.1: *Optimized CASSCF geometries:* ^{a} *The bond distances (in Å) and angles (in deg) are compared with the experimental and DFT (B3LYP) data for the electronic ground state (*C_{ip} *and* C_{op} *stand for the in-plane and out-of-plane carbon atoms in the* C_S*(yz) symmetry).* ^{b} *Reference [45].* ^{c} *References [120] and [47] respectively.* ^{d} *The values in parentheses are obtained with the 10e10a CASSCF active space.* ^{e} *Values after 20 cycles of optimization.* ^{f} *Average values.*

Both CASSCF and DFT optimized bond lengths and bond angles compare rather well to the experimental structures. The agreement between the experimental, the DFT and the CASSCF optimized structures for the electronic ground state validates the CASSCF active space which has to include the main bonding interactions in the complex. As mentioned in the previous section, two different CASSCF active spaces have been used, namely the 10e10a which excludes the four low-lying π^*_{CO} orbitals of the 10e14a adapted to the excited states calculations (see section 3.1). The largest deviation which never exceeds 5 % is obtained for the average Mn-C$_{ring}$ distance and the Mn-C$_{op}$ distance which are both very sensitive to the CASSCF active space. Indeed, when the π^*_{CO} orbitals are included in the active space the d$_\pi$-p$_\pi$ Mn-CO backdonation is well described (see the Mn-CO bond lengths which agree perfectly with the gas-phase determined values). Consequently, the Mn-Cp interaction governed by the $\pi_{Cp}/3d_{Mn}$ stabilizing interaction is significantly affected when going from the CAS10e10a to the CAS10e14a calculation (significant elongation of the calculated Mn-C$_{ring}$ distance). In any case, this interaction is underestimated either by the DFT method (Mn-C$_{ring}$=2.203 Å) or by the CASSCF method (2.231 Å or 2.215 Å) as compared to the experimental value of 2.149 Å reported in gas phase.

On the basis of the results obtained for the a^1A' state, the change of the geometry when going from the electronic ground state to the low-lying singlet excited states b^1A', c^1A' and d^1A' has been investigated through CASSCF calculations. The optimization of the c^1A' state did not converge to a minimum probably due to the dissociative character of this state. The values reported in Table 3.1 are the bond lengths and bond angles after 20 cycles of optimization. The main feature is a significant elongation of the Mn-C_{CO} distance of the in-plane carbonyl accompanied by the opening of the bond angle between the two out-of-plane carbonyls. The Mn-Cp and Mn-CO (out-of-plane) bonds are not significantly affected in this excited state. In order to confirm the dissociative character of the c^1A' state with respect to the in-plane carbonyl loss, potential energy curves have to be taken into account.

In section 3.5 it can be seen that at the MR-CCI level of theory it is the b^1A' and not the c^1A' state which has dissociative character. This is due to a crossing between the latter two states around the Frank-Condon region. The b^1A' optimized (CASSCF) structure which is very similar to the electronic ground state geometry should therefore correspond to the c^1A' MR-CCI state, whose potential shows a clear barrier in figure 3.3, due to further crossings with other states. The MR-CCI potential of the d^1A' state has a minimum along the Mn-CO stretching coordinate (figure 3.3) and its optimized structure does not differ much from the ground state one. The elongation of the Mn-CO bonds does not exceed 10 $\%$ in the b^1A' and d^1A' state and the Mn-Cp bond is not affected when exciting the molecule.

3.2.2 Structure of the fragment η^5-CpMn(CO)$_2$

The fragment η_5-CpMn(CO)$_2$ has been optimized at the DFT (B3LYP) level in the singlet closed-shell and triplet electronic configurations. The optimized structures are depicted in Figure 3.1.

As reported in ref [121], the DFT results show a lower energy for the triplet η^5-CpMn(CO)$_2$ relative to the singlet with ΔE = E$_{singlet}$ - E$_{triplet}$ = 8.09 kcal/mol (0.35 eV). We also found a lower DFT energy for the triplet with ΔE = 5.6 kcal/mol (0.24 eV). The lower energy of the triplet is in agreement with CASPT2 results (performed at the DFT optimized structure) [121]. On the contrary, MP2 results predict a lower energy of the singlet with ΔE=-10.93 kcal/mol (-0.47 eV) [121]. These results point to the near-degeneracy of the two electronic configurations in the unsaturated fragment.

When going from the reactant CpMn(CO)$_3$ electronic ground state to the low-lying singlet state of CpMn(CO)$_2$ the main deformation is a shortening of the Mn-Cp bond (ca. 20 $\%$) due to the enhancement of the Cp/Mn interaction after the

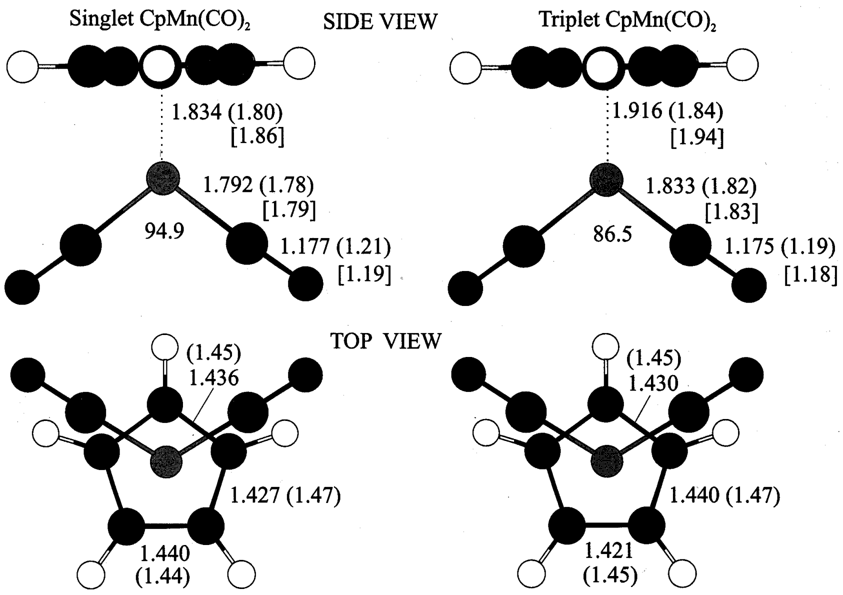

Figure 3.1: *Side and top views of the optimized geometries for the singlet and triplet CpMnCO$_2$. Bond distances in Å and angles in degrees. Values in parentheses and brackets correspond to MP2/lanl2dz and B3LYP/lanl2dz, respectively, from ref [121].*

loss of the CO ligand in the symmetry plane of CpMn(CO)$_3$. The C$_S$ symmetry is retained in the fragment. This justifies the model described in section 3.5: The potentials presented in this section are calculated under C$_S$ symmetry constraint and describe the cleavage of the in plane Mn-CO bond. The shortening of the Mn-Cp bond is also observed, to a lesser extent, in the triplet state which presents an important angular deformation with respect both to the singlet and to the reactant CpMn(CO)$_3$. According to recent geometry optimizations performed at the DFT level without any symmetry constraints the CpMn(CO)$_2$ fragment has also a geometry very close to C$_S$ symmetry [122].

3.3 CASSCF/CASPT2 and TD-DFT vertical excitation spectrum

The calculated B3LYP and BP86 excitation energies of the low-lying singlet electronic states of A' and A'' symmetry and the associated oscillator strengths are reported in Table 3.2. The lowest part of the absorption spectrum (below 31 000 cm^{-1} or 322 nm) is composed of metal centered transitions corresponding to 3d$_{Mn}$ to 3d$_{Mn}$ excitations. This is confirmed by the CASSCF/MS-CASPT2 excitation energies reported in Table 3.3. The excited states have a mixed character as docu-

B3LYP				BP86			
Transition	Principal configurations	ΔE	f		Principal configuration	ΔE	f
$a^1A' \rightarrow a^1A''$	$3d_{xy} \rightarrow 3d_{yz}$ (-0.43) $3d_{x2-y2} \rightarrow 3d_{xz}$ (0.48)	25200 (3.15)	0.0000	$a^1A' \rightarrow a^1A''$	$3d_{x2-y2} \rightarrow 3d_{xz}$ (0.54) $3d_{xy} \rightarrow 3d_{yz}$ (-0.47)	26480 (3.31)	0.0000
$a^1A' \rightarrow b^1A'$	$3d_{xy} \rightarrow 3d_{xz}$ (0.53) $3d_{x2-y2} \rightarrow 3d_{yz}$ (0.34)	26720 (3.34)	0.0097	$a^1A' \rightarrow b^1A'$	$3d_{xy} \rightarrow 3d_{xz}$ (0.55) $3d_{x2-y2} \rightarrow 3d_{yz}$ (0.39)	27760 (3.47)	0.0114
$a^1A' \rightarrow b^1A''$	$3d_{z2} \rightarrow 3d_{xz}$ (0.47) $3d_{xy} \rightarrow 3d_{yz}$ (0.31) $3d_{x2-y2} \rightarrow 3d_{xz}$ (0.27)	27040 (3.38)	0.0018	$a^1A' \rightarrow b^1A''$	$3d_{xy} \rightarrow 3d_{yz}$ (0.42) $3d_{z2} \rightarrow 3d_{xz}$ (0.38) $3d_{x2-y2} \rightarrow 3d_{xz}$ (0.35)	28800 (3.60)	0.0032
$a^1A' \rightarrow c^1A'$	$3d_{z2} \rightarrow 3d_{yz}$ (0.42) $3d_{x2-y2} \rightarrow 3d_{yz}$ (-0.42)	27240 (3.41)	0.0025	$a^1A' \rightarrow c^1A'$	$3d_{x2-y2} \rightarrow 3d_{yz}$ (0.48) $3d_{z2} \rightarrow 3d_{yz}$ (-0.32) $3d_{xy} \rightarrow 3d_{xz}$ (-0.32)	28880 (3.61)	0.0035
$a^1A' \rightarrow c^1A''$	$3d_{z2} \rightarrow 3d_{xz}$ (0.45) $3d_{xy} \rightarrow 3d_{yz}$ (-0.31) $3d_{x2-y2} \rightarrow 3d_{xz}$ (-0.29)	30720 (3.84)	0.0000	$a^1A' \rightarrow c^1A''$	$3d_{z2} \rightarrow 3d_{xz}$ (0.55) $3d_{xy} \rightarrow 3d_{yz}$ (-0.25) $3d_{x2-y2} \rightarrow 3d_{xz}$ (-0.23)	30400 (3.80)	0.0000
$a^1A' \rightarrow d^1A'$	$3d_{z2} \rightarrow 3d_{yz}$ (0.48) $3d_{x2-y2} \rightarrow 3d_{yz}$ (0.29) $3d_{xy} \rightarrow 3d_{xz}$ (-0.26)	30960 9(3.87)	0.0000	$a^1A' \rightarrow d^1A'$	$3d_{z2} \rightarrow 3d_{yz}$ (0.59) $3d_{x2-y2} \rightarrow 3d_{yz}$ (0.22) $3d_{xy} \rightarrow 3d_{xz}$ (-0.18)	30720 (3.84)	0.0001
$a^1A' \rightarrow d^1A''$	$3d_{xy} \rightarrow \pi^*_{CO}$(0.67)	33200 (4.15)	0.0005	$a^1A' \rightarrow d^1A''$	$3d_{xy} \rightarrow \pi^*_{CO}$(0.67)	34240 (4.28)	0.0004
$a^1A' \rightarrow e^1A'$	$3d_{x2-y2} \rightarrow \pi^*_{CO}$(0.66)	33200 (4.15)	0.0000	$a^1A' \rightarrow e^1A'$	$3d_{x2-y2} \rightarrow \pi^*_{CO}$(0.67)	34240 (4.28)	0.0005
$a^1A' \rightarrow e^1A''$	$3d_{xy} \rightarrow \pi^*_{CO}$(0.52) $3d_{x2-y2} \rightarrow \pi^*_{CO}$(-0.37)	36240 (4.53)	0.0003	$a^1A' \rightarrow e^1A''$	$3d_{xy} \rightarrow \pi^*_{CO}$(0.59) $3d_{x2-y2} \rightarrow \pi^*_{CO}$(-0.39)	37200 (4.65)	0.0002
$a^1A' \rightarrow f^1A''$	$3d_{x2-y2} \rightarrow \pi^*_{CO}$(0.54) $3d_{xy} \rightarrow \pi^*_{CO}$(0.38)	36800 (4.60)	0.0113	$a^1A' \rightarrow f^1A'$	$3d_{x2-y2} \rightarrow \pi^*_{CO}$(0.45) $3d_{xy} \rightarrow \pi^*_{CO}$(-0.37)	37440 (4.68)	0.0014
$a^1A' \rightarrow f^1A'$	$3d_{xy} \rightarrow \pi^*_{CO}$(0.46) $3d_{x2-y2} \rightarrow \pi^*_{CO}$(-0.47)	36800 (4.60)	0.0132	$a^1A' \rightarrow f^1A''$	$3d_{x2-y2} \rightarrow \pi^*_{CO}$(0.51) $3d_{xy} \rightarrow \pi^*_{CO}$(0.29) $3d_{xy} \rightarrow \pi^*_{CO}$(0.27)	37600 (4.70)	0.0024
$a^1A' \rightarrow g^1A'$	$3d_{z2} \rightarrow \pi^*_{CO}$(0.57) $3d_{xy} \rightarrow \pi^*_{CO}$(-0.26) $3d_{x2-y2} \rightarrow \pi^*_{CO}$(-0.25)	39840 (4.98)	0.0207	$a^1A' \rightarrow g^1A'$	$3d_{x2-y2} \rightarrow \pi^*_{CO}$(0.40) $3d_{x2-y2} \rightarrow \pi^*_{CO}$(-0.33) $3d_{x2-y2} \rightarrow \pi^*_{CO}$(0.31) $3d_{z2} \rightarrow \pi^*_{CO}$(0.25)	37680 (4.71)	0.0011

Table 3.2: *Calculated B3LYB and BP86 excitation energies in cm^{-1} (and eV) together with the corresponding one-electron excitations (weighting coefficients in parentheses) and oscillator strengths, f.*

mented by the CI coefficients of the principal configurations which do not exceed 0.5 in most cases. The $a^1A' \rightarrow b^1A'$, $a^1A' \rightarrow c^1A'$ and $a^1A' \rightarrow d^1A'$ transitions corresponding to $3d_{Mn} \rightarrow 3d_{Mn}$ excitations at 25 733cm^{-1}, 26 470 cm^{-1} and 30 366 cm^{-1}, respectively at the MS-CASPT2 level and at 26 720 cm^{-1} (27 760 cm^{-1}), 27 240 cm^{-1} (28 880 cm^{-1}) and 30 960 cm^{-1} (30 720 cm^{-1}), respectively at the DFT level (values obtained with the BP86 functional are given in parenthesis) contribute to the first shoulder of the absorption spectrum (*cf* figure 1.8) starting at 25 000 cm^{-1} (400 nm, 3.10 eV) with a maximum at 29 412 cm^{-1} (340 nm, 3.65 eV) [46].

To a lesser extent, the $a^1A' \rightarrow a^1A''$, $a^1A' \rightarrow b^1A''$ and $a^1A' \rightarrow c^1A''$ transitions corresponding to $3d_{Mn} \rightarrow 3d_{Mn}$ excitations between 24 972 cm^{-1} and 29 949 cm^{-1} at the MS-CASPT2 level and between 25 200 cm^{-1} and 30 720 cm^{-1} at the DFT level (B3LYP) should also contribute to this first band. The four low-lying singlet states of CpMn(CO)$_3$ are nearly degenerate and should contribute to the main UV absorption of this molecule according to the qualitative oscillator strengths reported in Tables 3.2 and 3.3. The experimental spectrum does not show

Transition	Principal configurations	CASSCF	MS-CASPT2	ω	f
a^1A'				0.733	
$a^1A' \rightarrow a^1A''$	$3d_{z2} \rightarrow 3d_{xz}$ (0.42) $3d_{xy} \rightarrow 3d_{yz}$ (0.44)	32021 (3.97)	24972 (3.10)	0.723	0.0110
$a^1A' \rightarrow b^1A'$	$3d_{xy} \rightarrow 3d_{xz}$ (-0.51) $3d_{x2-y2} \rightarrow 3d_{yz}$ (0.46)	34678 (4.33)	25733 (3.22)	0.721	0.0069
$a^1A' \rightarrow b^1A''$	$3d_{x2-y2} \rightarrow 3d_{xz}$ (0.68)	30779 (3.82)	26024 (3.23)	0.726	0.0085
$a^1A' \rightarrow c^1A'$	$3d_{z2} \rightarrow 3d_{yz}$ (~0.9)	32488 (4.06)	26470 (3.30)	0.724	0.0157
$a^1A' \rightarrow c^1A''$	$3d_{x2-y2}/3d_{z2} \rightarrow 3d_{xz}$ (0.55) $3d_{xy} \rightarrow 3d_{yz}$(-0.37)	37882 (4.70)	29949 (3.71)	0.720	0.0002
$a^1A' \rightarrow d^1A'$	$3d_{x2-y2}/3d_{z2} \rightarrow 3d_{yz}$ (0.56) $3d_{xy} \rightarrow 3d_{xz}$(0.42)	38396 (4.80)	30366 (3.80)	0.722	0.0015
$a^1A' \rightarrow e^1A'$	$3d_{x2-y2} \rightarrow \pi^*_{CO}$ (-0.57) $3d_{z2}/ 3d_{x2-y2} \rightarrow \pi^*_{CO}$ (0.41)	41149 (5.14)	36075 (4.51)	0.724	0.0000
$a^1A' \rightarrow d^1A''$	$3d_{xy} \rightarrow \pi^*_{CO}$ (-0.74)	40249 (4.99)	37410 (4.63)	0.727	0.0001
$a^1A' \rightarrow f^1A'$	$3d_{xy} \rightarrow \pi^*_{CO}$ (0.63) $3d_{z2} \rightarrow \pi^*_{CO}$ (0.42)	47733 (5.91)	40690 (5.09	0.720	0.0040
$a^1A' \rightarrow g^1A'$	$3d_{xy} \rightarrow \pi^*_{CO}$ (0.72) $3d_{z2} \rightarrow \pi^*_{CO}$ (-0.21)	46629 (5.80)	41175 (5.15)	0.723	0.0052
$a^1A' \rightarrow e^1A''$	$3d_{x2-y2} \rightarrow \pi^*_{CO}$ (0.83) $3d_{z2} \rightarrow \pi^*_{CO}$ (0.21)	43278 (5.37)	42346 (5.25)	0.730	0.0000
$a^1A' \rightarrow f^1A''$	$3d_{z2} \rightarrow \pi^*_{CO}$ (-0.82)	47939 (5.94)	45019 (5.58)	0.727	0.0004

Table 3.3: *Calculated CASSCF and MS-CASPT2 excitation energies in cm^{-1} (and eV) with corresponding one-electron excitation (weighting coefficients given in parentheses), weight coefficient of the reference CASSCF function ω in the perturbation method CASPT2, and CASSCF oscillator strengths f.*

any absorption around 34 482 cm^{-1} (290 nm, 4.28 eV) but a second band with a rather high intensity occurs with a peak around 40 000 cm^{-1} (250 nm, 4.96 eV).

The second band can be assigned to the $a^1A' \rightarrow f^1A'$ and $a^1A' \rightarrow g^1A'$ transitions corresponding to 3d$_{Mn} \rightarrow \pi^*_{CO}$ excitations at 40 690 cm^{-1} and 41 175 cm^{-1}, respectively at the MS-CASPT2 level. The $a^1A' \rightarrow e^1A'$ (36 075 cm^{-1}), $a^1A' \rightarrow d^1A'$ (37 410 cm^{-1}) , $a^1A' \rightarrow e^1A''$ (42 346 cm^{-1}) and $a^1A' \rightarrow f^1A''$ (45 019 cm^{-1}) have very low oscillator strengths and should contribute less significantly to this second band. The TD-DFT excitation energies of the $^1A'$ (3d$_{Mn}$ $\rightarrow \pi^*_{CO}$) excited states are calculated at 33 200 cm^{-1} (34 240 cm^{-1}), 36 800 cm^{-1} (37 600 cm^{-1}) and 39 840 cm^{-1} (37 680 cm^{-1}) and differ from the MS-CASPT2 values by more than 2000 cm^{-1}.

Even though the energetics obtained through the different methods compare rather well, the correlation between the CASSCF and the TD-DFT expansions is difficult to establish in some cases and some inconsistency remains at this level, as illustrated by the comparison given in table 3.4. As pointed out in section 2.8.2 a direct comparison between DFT and Hartree-Fock results is hazardous at mo-

	b^{1}A'			c^{1}A'			d^{1}A'		
	CASPT2	B3LYP	BP86	CASPT2	B3LYP	BP86	CASPT2	B3LYP	BP86
Excitation energies (cm^{-1})	25 733	26 720	27 760	26 470	27 240	28 880	30 366	30 960	30 720
Oscillator strengths	0.0069	0.0097	0.0114	0.0157	0.0025	0.0035	0.0015	0.0	0.0001
$3d_{xy} \rightarrow 3d_{xz}$	-.51	.53	.55	-	-	-.32	.42	-.26	-.18
$3d_{x2-y2} \rightarrow 3d_{yz}$	.46	.34	.39	-	-.42	.48	.28	.29	.22
$3d_{z2} \rightarrow 3d_{yz}$	-	-	-	.90	.42	-.32	.28	.48	.59
		e^{1}A'			f^{1}A'			g^{1}A'	
	CASPT2	B3LYP	BP86	CASPT2	B3LYP	BP86	CASPT2	B3LYP	BP86
Excitation energies (cm^{-1})	36 075	33 200	34 240	41 175	36 800	37 440	40 690	39 840	37 680
Oscillator strengths	0.0	0.0	0.0005	0.0052	0.0132	0.0014	0.004	0.0207	0.0011
$3d_{xy} \rightarrow \pi^*_{CO}$	-	-	-	.72	.46	-.37	.63	-.26	-
$3d_{x2-y2} \rightarrow \pi^*_{CO}$	-.57	.66	.67	-	-.47	.45	-	-.25	.40
$3d_{z2} \rightarrow \pi^*_{CO}$	.41	-	-	-.21	-	-	.42	.57	.25

Table 3.4: *Low-lying excited states calculated at the CASSCF/MS-CASPT2 and TD-DFT levels of theory.*

lecular orbitals level for both sets of orbitals obey different equations - the Kohn-Sham equations and the Hartree-Fock equations, respectively. The same holds for a comparison of DFT and CASSCF/CASPT2 which is based on Hartree-Fock theory. This leads to different coefficients for the principal orbital excitations of the different excited states. Nevertheless, both the TD-DFT and the CASPT2 methods agree in assigning $d-d$ transitions to the energetically lower states b^1A', c^1A' and d^1A' and $d-\pi^*_{CO}$ excitations to the energetically higher states e^1A', f^1A' and g^1A'. The agreement of the oscillator strengths f is reasonable for the b^1A', the d^1A' and the e^1A' states. For the other states the differences between the CASSCF and the DFT values on the one hand (c^1A') and the B3LYP and BP86 on the other hand (f^1A' and g^1A') are rather large.

In a recent paper [123] some general trends have been extracted from a comparative study performed on the electronic spectra of a number of unsaturated organic molecules. In particular the difficulty in describing charge transfer states in a dipeptide model has been attributed to insufficient flexibility in the functionals to describe states with extensive charge separations.

3.4 Comparison with MRCI excitation energies

According to the MS-CASPT2 and TD-DFT calculations of the last section the six low-lying metal-centered states of CpMn(CO)$_3$ range between 25 000 cm-1 and 30 000 cm-1 (3.13 eV- 3.80 eV), some of them being nearly degenerate around the Franck-Condon geometry. These states have been assigned to the absorption band observed in the experimental spectrum between 400 nm and 290 nm (3.10 eV-4.28 eV). The MR-CCI transition energies obtained in this work are reported in table 3.5

together with the MS-CASPT2 and TD-DFT values calculated in the previous section. For instance, the b^1A' and c^1A' have been calculated at 25 730 cm^{-1} and 26 470 cm^{-1}, respectively at the MS-CASPT2 level (26 720 cm^{-1} and 27 240 cm^{-1} at the TD-DFT level) and 25 840 cm^{-1} and 28 400 cm^{-1} at the MR-CCI level. The overall agreement between the different levels of calculation is satisfactory. The largest deviations between the MR-CCI and MS-CASPT2 values, obtained for the b^1A'' and c^1A' states amount to 1180 cm^{-1} and 1930 cm^{-1}, respectively. The corresponding deviations between the MRCCI and TD-DFT transitions energies amount to 160 cm^{-1} and 1160 cm^{-1}, respectively. The transition energies obtained through the MR-CCI approach are generally overestimated with respect to the MS-CASPT2 transitions energies. These trends have been observed and discussed for other transition metal complexes [124, 125]. It is generally difficult to conclude about the relative quality of the two approaches since this depends strongly on the zeroth-order wavefunction given by the CASSCF calculation. Indeed the reference wavefunction has not to fulfill exactly the same criteria for assuring a balanced description of the different excited states depending on whether the remaining electronic correlation is added perturbationally (CASPT2) or variationally (MR-CCI). However, the overall agreement between the different methods validates the use of the MR-CCI method for the computation of the potential energy curves associated with the low-lying singlet excited states of CpMn(CO)$_3$.

Transition	MR-CCI	MS-CASPT2	TD-DFT(B3LYP)
$a^1A' \rightarrow a^1A''$	25 040 (3.13)	24 970 (3.10)	25 200 (3.15)
$a^1A' \rightarrow b^1A'$	25 840 (3.23)	25 730 (3.22)	26 720 (3.34)
$a^1A' \rightarrow b^1A''$	27 200 (3.40)	26 020 (3.25)	27 040 (3.38)
$a^1A' \rightarrow c^1A'$	28 400 (3.55)	26 470 (3.31)	27 240 (3.41)
$a^1A' \rightarrow c^1A''$	33 600 (4.20)	29 950 (3.71)	30 720 (3.84)
$a^1A' \rightarrow d^1A'$	33 600 (4.20)	30 370 (3.80)	30 960 (3.87)
$a^1A' \rightarrow d^1A''$	35 600 (4.45)	-	-

Table 3.5: *Transition energies (in cm^{-1} and eV) to the low-lying $^1A'$ and $^1A''$ excited states of CpMn(CO)$_3$ at different levels of calculations (MR-CCI, MS-CASPT2 and TD-DFT).*

3.5 CASSCF/MR-CCI potential curves and transition dipole moments

The potential energy curves have been computed under the assumption that the C_S symmetry is retained along the reaction path corresponding to the CO_{ax} loss (figure 3.2) and the fragment $CpMn(CO)_2$ is kept frozen in the Franck-Condon geometry.

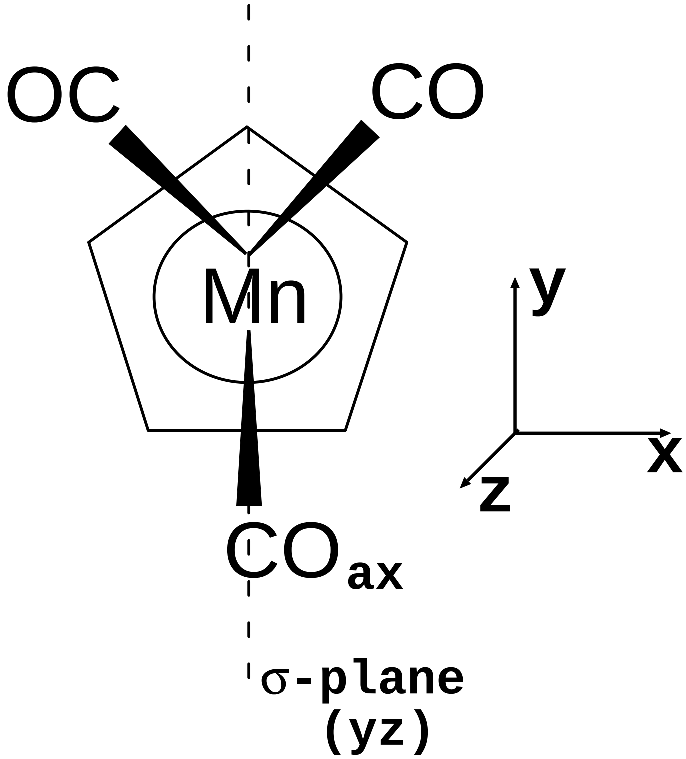

Figure 3.2: *Model system used in the calculations of the potential energy curves.*

This is in reasonable agreement with the DFT geometry optimizations reported in section 3.2.2 which show a symmetry of the $CpMn(CO)_2$ fragment very close to C_S. Furthermore, these assumptions are justified by the time-scale of the primary photoprocess investigated in this work, namely the CO loss which occurs within a few tens of femtoseconds [24].

The one-dimensional potential energy curves $V(q_a)$ (with q_a=[Mn-CO_{ax}]) for the electronic ground state potential a^1A' and the b^1A', c^1A', d^1A', e^1A' and a^1A'', b^1A'', c^1A'' and d^1A'' states have been obtained through CASSCF calculations supplemented by a MR-CCI treatment and are shown in figure 3.3. They correspond to single excitations from the $3d_{Mn}$ to the $3d_{xz}$ and $3d_{yz}$ orbitals of symmetry a' and a'', respectively.

Average CASSCF calculations (with equal weights) over 4 roots for the $^1A'$ states and 4 roots for the $^1A''$ states were performed to obtain electronic wavefunc-

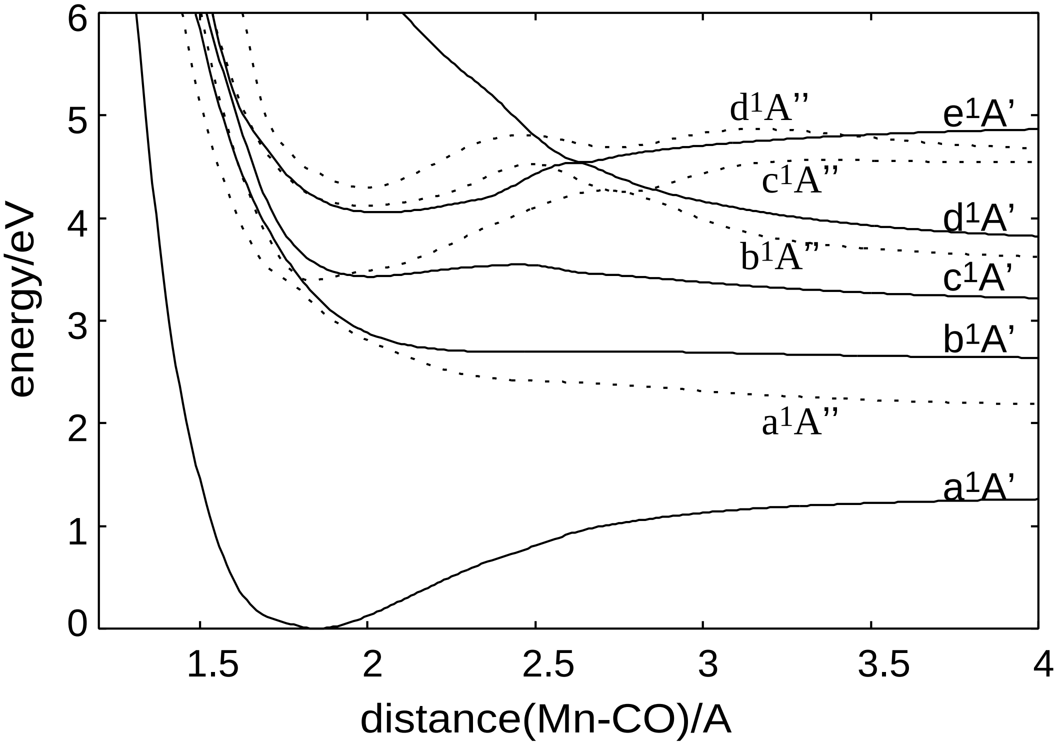

Figure 3.3: *CASSCF/MRCI adiabatic non-relaxed potential energy curves as a function of the Mn-CO$_{ax}$ elongation in CpMnCO$_3$, computed under C_S symmetry constraint.*

tions used as references in the subsequent MR-CCI calculations. The 10e14a active space described in section 3.2 was used to compute the CASSCF wave function. Single and double excitations to the whole virtual space were included in a multireference scheme keeping as references the configurations with CI coefficients larger than 0.08 for all roots. For the e^1A' state this was only possible at dissociation. Around the Franck-Condon region the e^1A' state corresponds to a much energetically higher state, not included in the reference CASSCF wavefunction. Because of converge problems in the MR-CCI treatment the energy of this state is overestimated in the Franck-Condon region. The dissociation barrier of the electronic ground a^1A' state is calculated to be 126.2 kJ/mol (1.34 eV). This value is in the range of the calculated values and experimental data available for the metal-carbonyl bond dissociation energy in first-row transition metal carbonyls [126].

The set of adiabatic potential energy curves depicted in figure 3.3 is characterized by several avoided crossings, two of them around the Franck-Condon geometry between the b^1A' and c^1A' and between the a^1A'' and b^1A'' both at ca. 1.8 Å. Whereas the b^1A'' potential appears to be dissociative leading directly to the primary products CO + MnCp(CO)$_2$ [b^1A'], the c^1A' presents a small energy barrier around 2.5 Å, due to an avoided crossing with d^1A', which will prevent fast and total dissociation. The a^1A'' and b^1A'' states which are nearly degenerate around the equilibrium geometry avoid each other at this point, leading to one dissociative potential towards the primary products CO + MnCp(CO)2 [a^1A''] and to a quasi-bound potential which will trap the molecular system. The upper states d^1A', e^1A', c^1A'' and d^1A'' have been calculated in order to get the main features of the absorption spectrum in the UV energy domain and to perform dynamical simulations which should take into account the non-adiabatic coupling between the different electronic states.

The electronic transition dipole moments (TDM), depicted in figure 3.4, were calculated at the MR-CCI level for the $^1A'$ states and at the CASSCF level for the $^1A''$ states. For the sake of comparison, TDMs have been also computed at CASSCF level for the A' states, and MR-CCI and CASSCF results are in reasonable agreement. For symmetry reasons (C$_S$) the x-component of the TDM connecting the A' states with the electronic ground state (a^1A') and the y- and z-component coupling the A'' states with the ground state vanish. Moreover, the absolute values of the y- and z-components corresponding to the $a^1A' \rightarrow b^1A'$ and the $a^1A' \rightarrow c^1A'$ excitations are quite different in the Franck-Condon region: The y-component for the $a^1A' \rightarrow b^1A'$ transition is much larger than that for the $a^1A' \rightarrow c^1A'$ excitation: TDM(y): $a^1A' \rightarrow b^1A' \gg$ TDM(y): $a^1A' \rightarrow c^1A'$, and the reverse holds for the z-component: TDM(z): $a^1A' \rightarrow b^1A' \ll$ TDM(z): $a^1A' \rightarrow c^1A'$. In the case of the x-component (excitation of A'' states) it is found that the absolute value of the $a^1A' \rightarrow a^1A''$ transition dipole is much larger than the one corresponding to the $a^1A' \rightarrow b^1A''$ excitation. These large differences of the transition dipole moments will have a strong influence on the wavepacket dynamics of the corresponding states (see chapter 4). Namely, if laser energies which populate only the lowest excited states of each symmetry are used the following dominant excitations can be expected:

x-polarized: b^1A'' mainly populated,

y-polarized: b^1A' mainly populated,

z-polarized: c^1A' mainly populated.

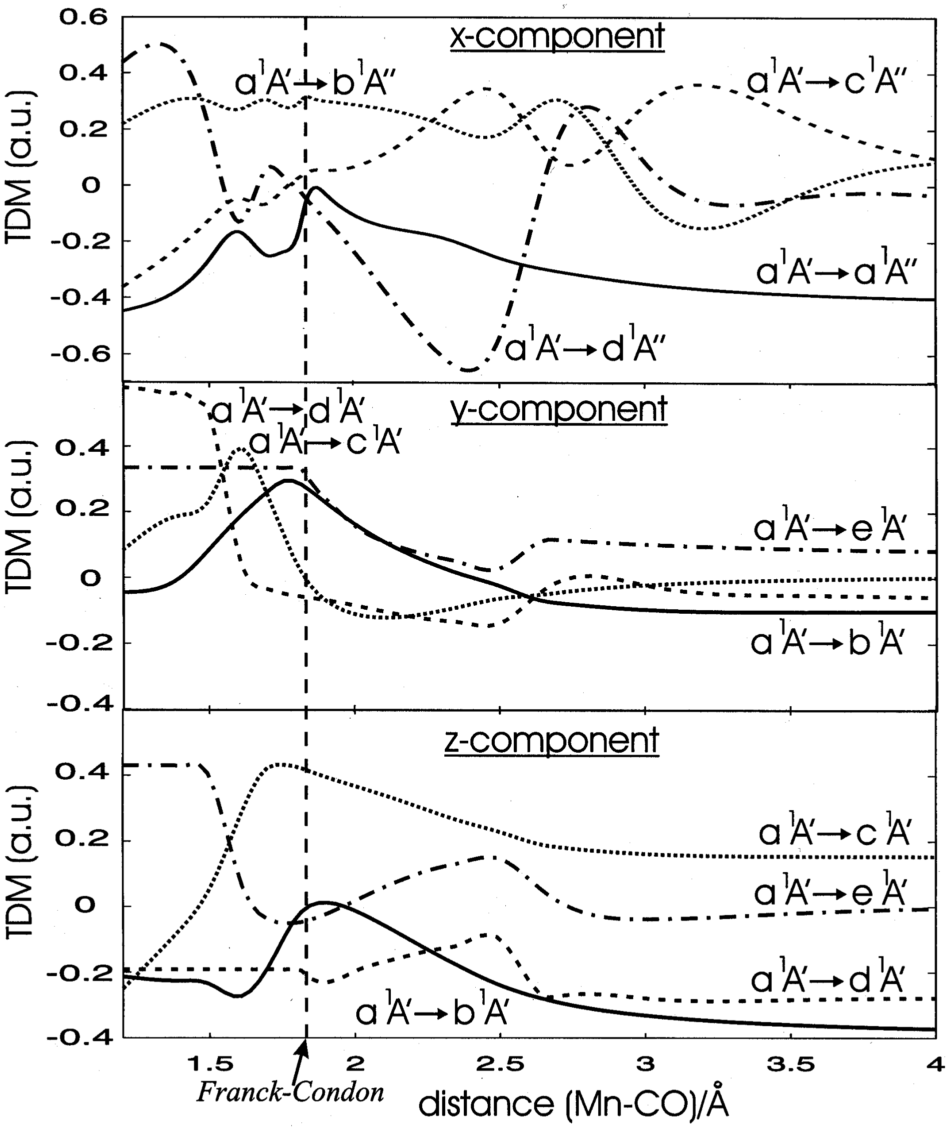

Figure 3.4: *X-, Y- and Z-components of the CASSCF/MR-CCI adiabatic electronic transition dipole moments in* $CpMnCO_3$ *(1 a.u. = 1* ea_0*).*

3.6 The kinetic couplings

The general properties of the kinetic coupling terms $T^{(1)}$ and $T^{(2)}$ are discussed in section 2.9. A way to approximately compute them using the coefficients of the CI expansion in a multiconfigurational wavefunction is described there. In the case of the potential energy curves of A' symmetry all couplings between the four low-lying excited states were calculated whereas for the A'' symmetry only those between the two lowest electronic states were taken into account. The estimated coupling elements here presented are only those between the b^1A' and c^1A' states and between the states a^1A'' and b^1A'', called α and β to distinguish from the A' states labeled a, b,... etc. All other calculated coupling elements are given in the appendix B.

3.6.1 The kinetic coupling term T$^{(1)}$

A'-states

The four low-lying excited states of symmetry A' are composed of four main configurations here denoted by D_1, D_2, D_3 and D_4. These configurations differ in the occupation of the highest occupied molecular orbitals for each symmetry, which are $21a'$, $22a'$ and $23a'$ for a'-symmetry, and $13a''$ and $14a''$ for a''-symmetry. In the ground state configuration the orbitals $21a'$, $22a'$ and $13a''$ are doubly occupied whereas the orbitals $23a'$ and $13a''$ are the lowest unoccupied orbitals. All considered molecular orbitals have mainly d-character. The orbitals $23a'$, $13a''$ and $14a''$ show a leading coefficient for one d-orbital: $23a'$ is mainly a d_{yz}-, $13a''$ a d_{xy}- and $14a''$ a d_{xz}-orbital. The orbitals $21a'$ and $22a'$ are linear combinations of a d_{z^2}- and a $d_{x^2-y^2}$-orbital. This assignment can be summarized as follows:

$$\begin{aligned}
21a' &\approx k_{21,z^2} \cdot d_{z^2} + k_{21,x^2-y^2} \cdot d_{x^2-y^2}, \\
22a' &\approx k_{22,z^2} \cdot d_{z^2} + k_{22,x^2-y^2} \cdot d_{x^2-y^2}, \\
23a' &\approx d_{yz}, \\
13a'' &\approx d_{xy}, \\
14a'' &\approx d_{xz}.
\end{aligned}$$

The determinants $D_{1...4}$ are characterized by the following occupation schemes:

$$D_1 : (21a')^1, (22a')^2, (23a')^1, (13a'')^2, (14a'')^0$$

$$D_2 : (21a')^2, (22a')^1, (23a')^1, (13a'')^2, (14a'')^0$$

$$D_3 : (21a')^2, (22a')^2, (23a')^0, (13a'')^1, (14a'')^1$$

$$D_4 : (21a')^2, (22a')^2, (23a')^2, (13a'')^0, (14a'')^0$$

These configurations are illustrated in figure 3.5.

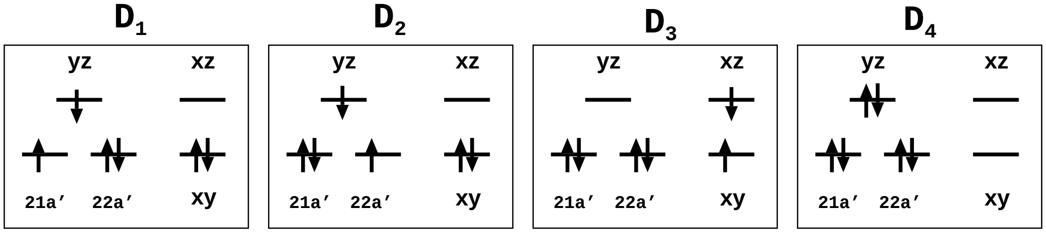

Figure 3.5: *Occupation schemes of the four leading configurations which describe the electronic excited states of symmetry A' .*

From these state configurations (figure 3.5) and applying the Condon-Slater rules it follows that,

$$\langle D_1(\underline{q_a})|\frac{\partial}{\partial q_a}D_4(\underline{q_a})\rangle = \langle D_2(\underline{q_a})|\frac{\partial}{\partial q_a}D_4(\underline{q_a})\rangle = \langle D_3(\underline{q_a})|\frac{\partial}{\partial q_a}D_4(\underline{q_a})\rangle$$

$$= \langle D_1(\underline{q_a})|\frac{\partial}{\partial q_a}D_3(\underline{q_a})\rangle = \langle D_2(\underline{q_a})|\frac{\partial}{\partial q_a}D_3(\underline{q_a})\rangle = 0.$$

and the only non-vanishing matrix elements are:

$$\langle D_1(\underline{q_a})|\frac{\partial}{\partial q_a}D_2(\underline{q_a})\rangle = -\langle D_2(\underline{q_a})|\frac{\partial}{\partial q_a}D_1(\underline{q_a})\rangle,$$

because only D_1 and D_2 differ in a single excitation, while the other matrix elements involve two or more electron exchanges. These elements can be easily calculated under the assumption that also the atomic orbitals are orthonormal and do not depend on q_a. Recalling the composition of the molecular orbitals 21 a' and 22 a', it is possible to write,

$$\tau_{12} = \langle D_1(\underline{q_a})|\frac{\partial}{\partial q_a}D_2(\underline{q_a})\rangle = \langle 22a'|\frac{\partial}{\partial q_a}21a'\rangle$$

$$= \langle k_{22,z^2} \cdot d_{z^2} + k_{22,x^2-y^2} \cdot d_{x^2-y^2}|\frac{\partial}{\partial q_a}\left(k_{21,z^2} \cdot d_{z^2} + k_{21,x^2-y^2} \cdot d_{x^2-y^2}\right)\rangle$$

$$\approx k_{22,z^2}\frac{\partial}{\partial q_a}k_{21,z^2} + k_{22,x^2-y^2}\frac{\partial}{\partial q_a}k_{21,x^2-y^2} \tag{3.1}$$

and

$$\tau_{21} = \langle D_2(\underline{q_a})|\frac{\partial}{\partial q_a}D_1(\underline{q_a})\rangle = -\tau_{12} = \langle 21a'|\frac{\partial}{\partial q_a}22a'\rangle$$

$$= \langle k_{21,z^2} \cdot d_{z^2} + k_{21,x^2-y^2} \cdot d_{x^2-y^2} | \frac{\partial}{\partial q_a} \left(k_{22,z^2} \cdot d_{z^2} + k_{22,x^2-y^2} \cdot d_{x^2-y^2} \right) \rangle$$

$$\approx k_{21,z^2} \frac{\partial}{\partial q_a} k_{22,z^2} + k_{21,x^2-y^2} \frac{\partial}{\partial q_a} k_{22,x^2-y^2}, \tag{3.2}$$

where k_{ij} are the corresponding coefficients of the molecular expansion. The shorthand notation used to label the states b^1A', c^1A', d^1A' and e^1A' is b, c, d and e respectively. In the top panel of table 3.6 the CI coefficients (*cf* equation (2.120)) of the states b, c, d and e corresponding to the determinants D_1, D_2, D_3 and D_4 are shown. Also the orbital coefficients k_{ij} are given in the top panel of table 3.6. From these data the kinetic coupling terms have been computed according to equation (2.121). Here only the terms which couple the b^1A' and the c^1A' state are shown. The results for all other terms are listed in appendix B. The data of table 3.6 were interpolated using a smooth cubic spline procedure with different standard deviations given in the figure captions. The CI coefficients are plotted in figures B.1 to B.4 of appendix B. The orbital coefficients are depicted in figure B.5. In some cases (see figure captions) points were omitted in order to get smooth curves. Note that in those cases the real curves would look steeper than the shown ones. The smoothed data were then used to calculate $T^{(1)}$ according to (2.121). The matrix elements $A^{(1)}_{bc}$ and $A^{(1)}_{cb}$ of the first term $A^{(1)}$ (*cf* eq. (2.121)) and the corresponding elements of the second term $B^{(1)}$ are shown in figure 3.6 (a) and 3.6 (b) respectively. All other matrix elements of $A^{(1)}$ and $B^{(1)}$ are given in the appendix: Figures B.6 to B.9 and figures B.10 to B.13 respectively. In figure 3.7, τ_{12} and τ_{21} resulting from the orbital change are plotted.

As derived in section 2.9.1 the resulting matrix elements should be antisymmetric. However, technically speaking they are not because of numerical errors. To get a precise antisymmetric matrix $T^{(1)}$, the calculated elements A_{ij} and -A_{ji} as well as τ_{12} and -τ_{21} have been averaged. Finally $T^{(1)}$ is the sum of $A^{(1)}$ and $B^{(1)}$. Its matrix elements for the coupling between the b and c state are shown in figure 3.8. All other matrix elements can be found in the appendix in the figures B.14 to B.17. Note that the matrix element $T^{(1)}_{be}$ is, within the error bar, zero along the reaction coordinate and therefore not shown.

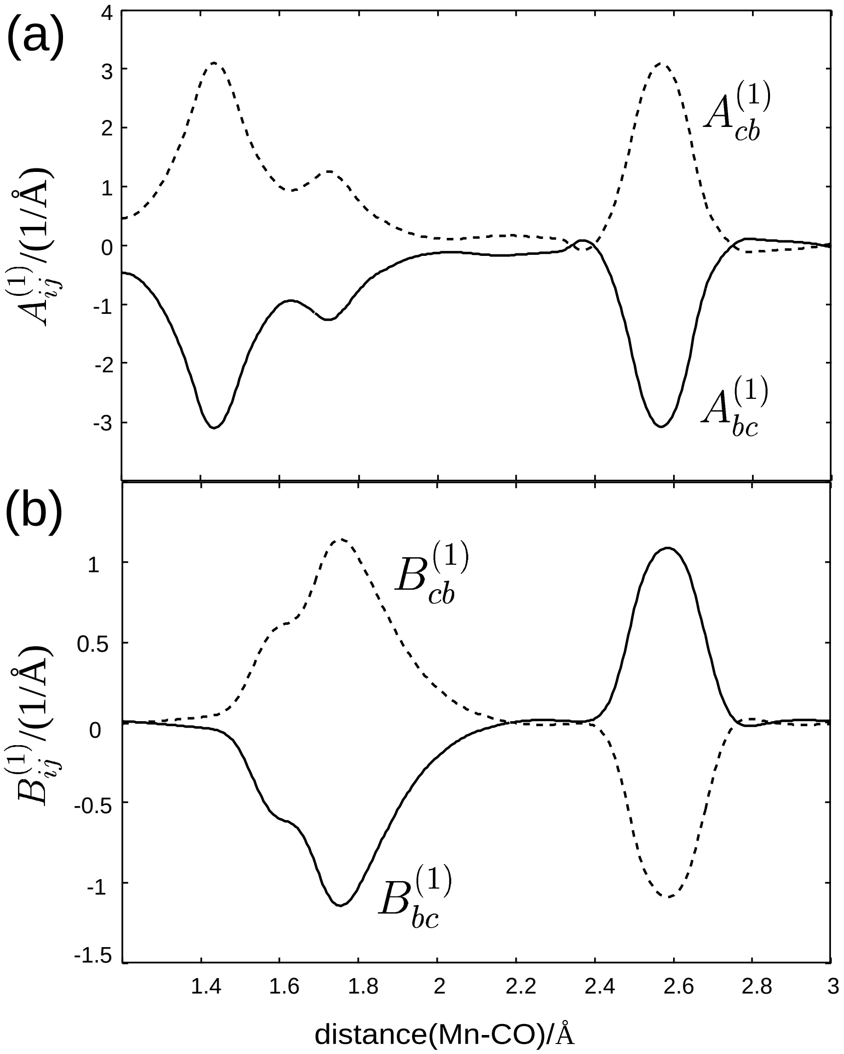

Figure 3.6: *Panel (a) shows the elements* $A^{(1)}_{bc}$ *and* $A^{(1)}_{cb}$ *calculated from the CI coefficients according to equation (2.121). Panel (b) shows the elements* $B^{(1)}_{bc}$ *and* $B^{(1)}_{cb}$ *calculated from the CI coefficients according to equation (2.121). The* A_{ij} *matrix elements (CI term) are larger than the corresponding* B_{ij} *elements (MO term) except around 1.8 Å, where they have approximatly the same values (*$\approx$ *1).*

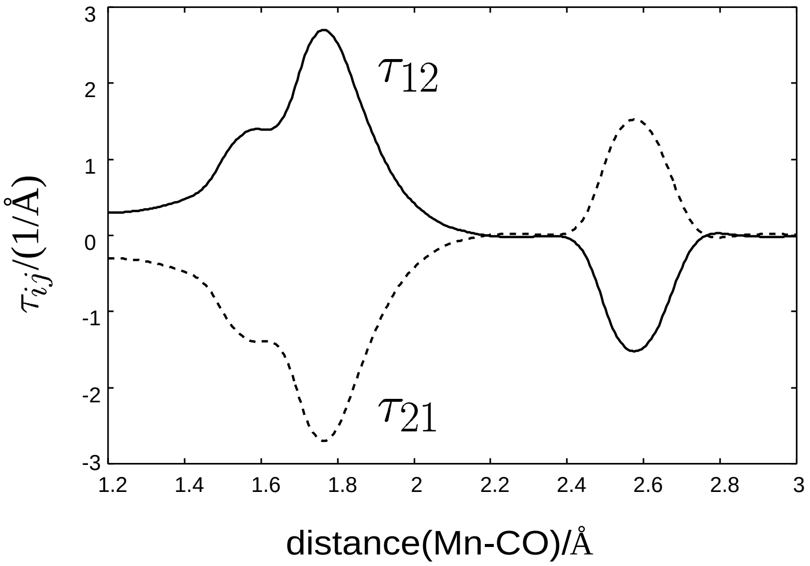

Figure 3.7: *Elements* τ_{12} *and* τ_{21} *calculated according to equations (3.1) and (3.2), respectively.*

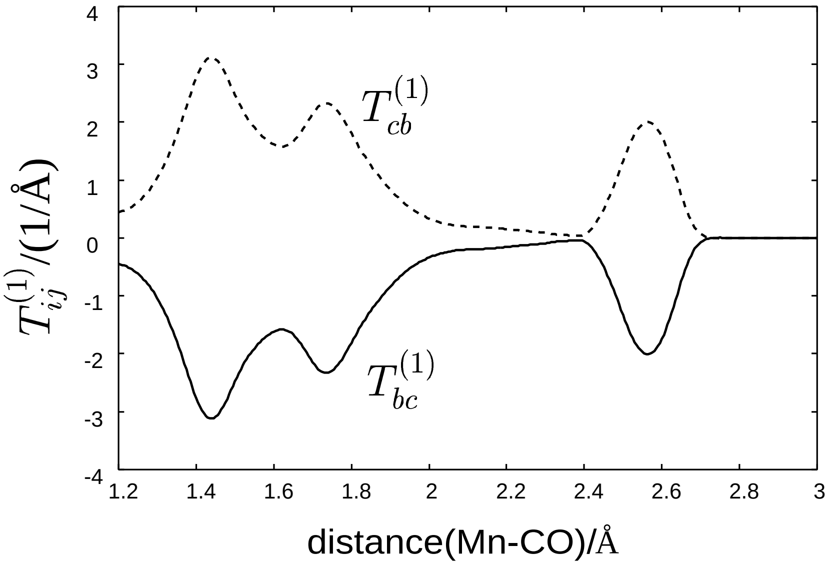

Figure 3.8: *Coupling element* $T_{bc}^{(1)}$ *and* $T_{cb}^{(1)}$ *calculated from the CI coefficients according to equation (2.121). The matrix elements of* $T^{(1)}$ *are the sum of the corresponding elements of* $A^{(1)}$ *(CI term) and* $B^{(1)}$ *(MO term) shown in figure 3.6. In the present case, both contributions are important.*

A''-states

In the case of the A''-states the orbitals are basically pure and they can thus be approximated by a single atomic basis function. The assignment of the relevant orbitals reads as follows:

$$\begin{aligned} 20a' &\approx d_{z^2}, \\ 21a' &\approx d_{x^2-y^2}, \\ 22a' &\approx \pi^*_{Cp}, \\ 23a' &\approx d_{yz}, \\ 24a' &\approx \pi^*_{CO}, \\ 13a'' &\approx d_{xy}, \\ 14a'' &\approx d_{xz}. \end{aligned}$$

Since the molecular orbitals are mainly described by single atomic orbitals, the electronic configurations with the dominant CI coefficients which describe the four low-lying excited states of symmetry A'' are easily described below. All excitations are d-d transitions except one which is a transition to a π^*_{CO}-orbital. This means that the excited states are completely determined by the occupation scheme of the d-orbitals and the π^*_{CO}-orbital:

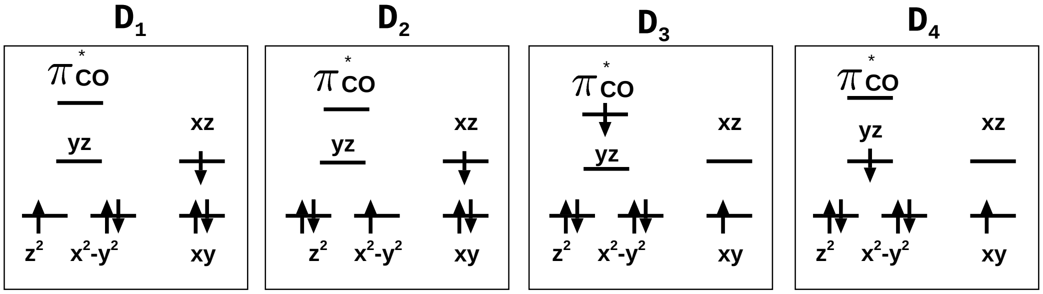

Figure 3.9: *Occupation schemes of the four leading configurations which describe the two lowest excited states of symmetry A'' till ca. 2.5 Å.*

$$D_1 : (d_{z^2})^1, (d_{x^2-y^2})^2, (d_{yz})^0, (\pi^*CO)^0, (d_{xy})^2, (d_{xz})^1 : \quad d_{z^2} \rightarrow d_{xz}$$

$$D_2 : (d_{z^2})^2, (d_{x^2-y^2})^1, (d_{yz})^0, (\pi^*CO)^0, (d_{xy})^2, (d_{xz})^1 : \quad d_{x^2-y^2} \rightarrow d_{xz}$$

$$D_3 : (d_{z^2})^2, (d_{x^2-y^2})^2, (d_{yz})^0, (\pi^*CO)^1, (d_{xy})^1, (d_{xz})^0 : \quad d_{xy} \rightarrow \pi^*CO$$

$$D_4 : (d_{z^2})^2, (d_{x^2-y^2})^2, (d_{yz})^1, (\pi^*CO)^0, (d_{xy})^1, (d_{xz})^0 : \quad d_{yz} \rightarrow d_{xy}$$

$$D_5 : (d_{z^2})^1, (d_{x^2-y^2})^2, (d_{yz})^2, (\pi^*CO)^0, (d_{xy})^1, (d_{xz})^0 : \quad \text{double excitation}$$

$$D_6 : (d_{z^2})^2, (d_{x^2-y^2})^1, (d_{yz})^2, (\pi^*CO)^0, (d_{xy})^1, (d_{xz})^0 : \quad \text{double excitation}$$

Note that the π^*_{Cp} $(22a')$ orbital remains doubly occupied in all considered configurations. Therefore, it is neither shown in figure 3.9 nor in the previous occupation scheme. However, from the CI coefficients (*cf* bottom panel of table 3.6) it can be seen that these configurations do not suffice to describe the excited states from the Frank-Condon window to the asymptotic region: Two states corresponding to the configurations D_5 and D_6 cross the b^1A'' adiabatic state after 2.5 Å. Single point calculations at the Frank-Condon geometry have shown that these intruding states are not the next two higher states at this point, as one could expect, but higher ones. For the purpose of simulating experiments with excitation energies around 3.1-3.6 eV, states with higher energies are not needed and it suffices to have the two lowest A'' states properly characterized. Wave packet propagations without kinetic coupling, described in section 4.4, will show that with the above mentioned excitation energies only the b^1A'' state is populated whereas the a^1A'' state stays nearly unpopulated because of the weakness of its transition dipole moment. In the b^1A'' state the wave packet is trapped and the a^1A'' can only be populated through a coupling between both excited states. According to table 3.6 the b^1A'' state is only well described till ca. 2.5 Å. This is however enough for a proper dynamics description, since the trapped wave packet in this state never reaches 2.5 Å. Below 2.5 Å the two low-lying states of symmetry A'' are well defined using four configurations. This can be seen from table 3.6 where the coefficients corresponding to this states, $C_{\alpha/\beta,1...4}$, are dominant till 2.5 Å . These four configurations are illustrated by the occupation schemes of the relevant orbitals in figure 3.9.

Likewise, the CI coefficients functions were interpolated by a cubic spline procedure. The resulting curves are given in the figures B.18 to B.19 of appendix B. In the case of the A'' states no molecular orbitals showing a strong mixing of two or more atomic basis functions (like in the A' case) occurred. For that reason the orbitals are assumed to keep constant during the Mn-CO bond elongation, and therefore the elements τ_{jk} and consequently the terms $B^{(1)}_{\mu\nu}$ in equation (2.121) vanish. This means that in the A'' case only the term $A_{\mu\nu}$ needs to be calculated to estimate $T^{(1)}_{\mu\nu}$. The resulting elements $T^{(1)}_{\alpha\beta}$ and $T^{(1)}_{\beta\alpha}$ are shown in figure 3.10. Again they were averaged to be antisymmetric.

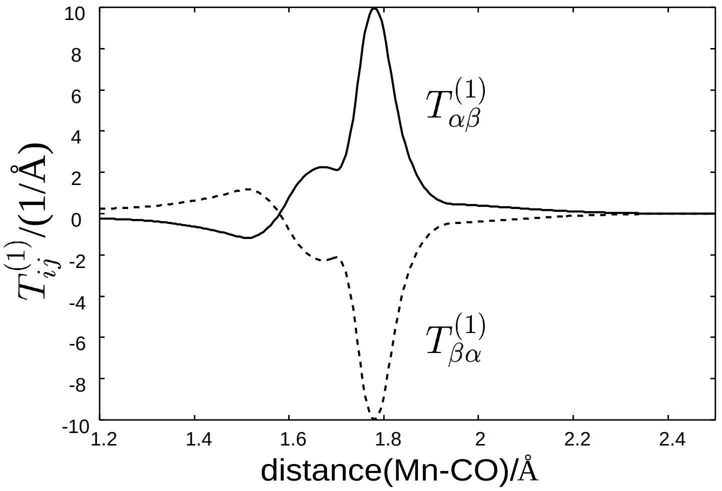

Figure 3.10: *Coupling elements $T^{(1)}_{\alpha\beta}$ and $T^{(1)}_{\beta\alpha}$ that couple the states a^1A'' (=α) and b^1A'' (=β) calculated from the CI coefficients according to equation (2.121).*

3.6.2 The kinetic coupling term $\mathbf{T}^{(\mathbf{2})}$

The kinetic coupling elements $\mathrm{T}^{(\mathbf{2})}$ have been calculated according to equation (2.126). In figure 3.11 the elements of $\underline{\underline{T}}^{(2)}$ that couple the b^1A' with the c^1A' state are shown and those which couple the a^1A'' and the b^1A'' state are plotted in figure 3.12. In the figures B.20 to B.23 of appendix B all other elements of $\underline{\underline{T}}^{(2)}$, for the case of A' symmetry are presented. It has to be noted that although $\underline{\underline{T}}^{(1)}$ has diagonal elements equal to zero this is not the case for $\underline{\underline{T}}^{(2)}$. The diagonal elements are shown in figure B.24 for A' symmetry and in figure B.25 for A'' symmetry. These matrix elements have to be added to the potential curves. But according to equation 2.21 $T^{(2)}$ must be multiplied with $\frac{\hbar^2}{2\mu_a}$. This leads to maxima of the diagonal elements of less than 0.01 eV and therefore negligible. Thus, they have not been included in the dynamical simulations. Also it should be pointed out that $\underline{\underline{T}}^{(2)}$ is not anti-symmetric (see section 2.9.1). Nevertheless, some elements look like anti-symmetric since the derivative term (which is indeed anti-symmetric) is dominant in these cases.

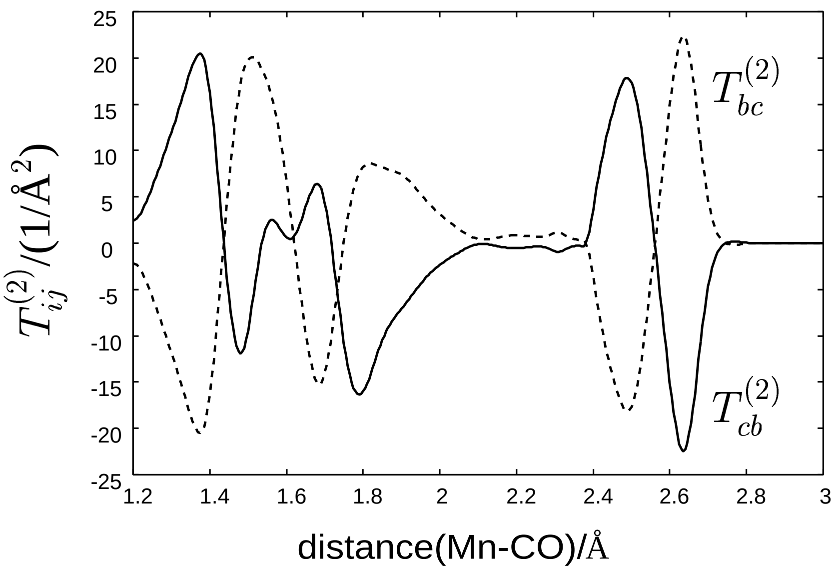

Figure 3.11: *Coupling element* $T_{bc}^{(2)}$ *and* $T_{cb}^{(2)}$ *calculated using the CI coefficients according to equation (2.126).*

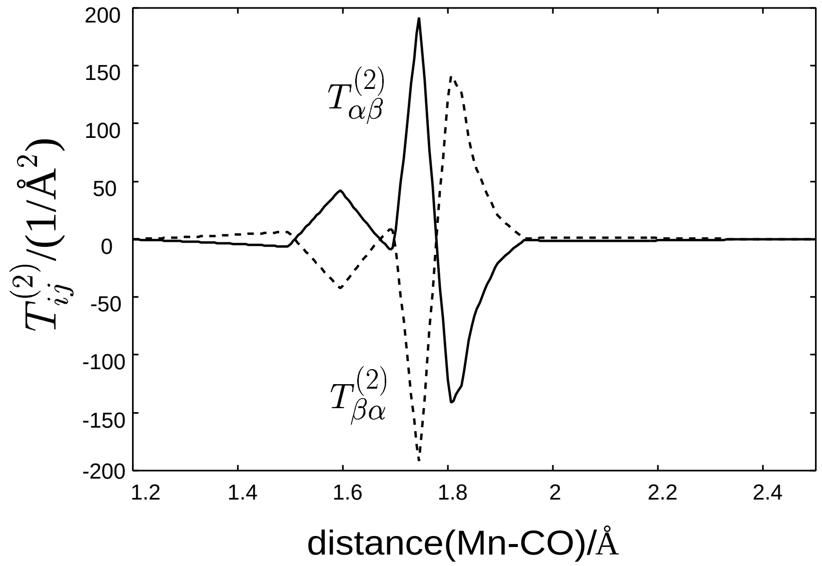

Figure 3.12: *Coupling elements* $T_{\alpha\beta}^{(2)}$ *and* $T_{\beta\alpha}^{(2)}$ *calculated using the CI coefficients according to equation (2.126).*

3.6.3 Source of errors

Our approach of calculating the kinetic coupling terms $T^{(\mathbf{1})}$ and $T^{(\mathbf{2})}$ using the CI and MO coefficients of a MR-CCI electronic wave function is based on a series of approximations. They lead to errors which have to be kept in mind:

1. Only the leading CI and the MO coefficients with largest changes have been taken into account in the calculation of the kinetic coupling term $T^{(\mathbf{1})}$.
2. In order to get smooth curves in the spline smoothing procedure not all the points have been considered (see appendix B).
3. For the calculation of $T^{(\mathbf{2})}$ according to equation (2.126) a complete basis is assumed. However, in practice the basis has not been complete.

Table 3.6:

Upper part: CI-coefficients $C_{\nu,j}$ of the states b^1A' (b), c^1A' (c), d^1A' (d), e^1A' (e) and orbital coefficients $k_{\nu,j}$ of the molecular orbitals $21a'$ (21) and $22a'$ (22) as a function of the Mn-CO distance q_a (in Å).
Lower part: CI-coefficients $C_{\nu,j}$ of the states a^1A'' (α), b^1A'' (β), c^1A'' (γ) and d^1A'' (δ) as a function of the Mn-CO distance q_a (in Å).

q_a/ Å	$C_{b,1}$	$C_{b,2}$	$C_{b,3}$	$C_{b,4}$	$C_{c,1}$	$C_{c,2}$	$C_{c,3}$	$C_{c,4}$	$C_{d,1}$	$C_{d,2}$	$C_{d,3}$	$C_{d,4}$	$C_{e,1}$	$C_{e,2}$	$C_{e,3}$	$C_{e,4}$	$k_{21,z2}$	$k_{21,x2-y2}$	$k_{22,z2}$	$k_{22,x2-y2}$				
1.20	0.02	+0.93	0.10	-0.0	-0.03	-0.09	0.93	0.0	0.92	0.01	0.02	-0.0	0.0	0.0	0.0	0.37	-0.51	-0.29	0.41	-0.48				
1.40	-0.09	+0.87	0.32	-0.0	0.12	-0.30	0.87	0.0	0.91	0.13	-0.08	-0.0	0.0	0.0	0.0	0.52	-0.45	-0.42	0.49	-0.43				
1.50	-0.08	0.70	0.61	0.0	0.30	-0.55	0.69	-0.0	0.87	0.26	-0.17	-0.0	0.0	0.0	0.0	0.82	-0.40	-0.48	0.54	-0.38				
1.60	-0.08	0.43	0.82	0.0	0.93	0.10	0.04	0.0	-0.06	0.82	-0.44	-0.0	0.0	0.0	0.0	0.60	-0.18	-0.59	0.65	-0.19				
1.70	0.016	0.52	0.78	-0.0	0.78	0.42	-0.29	0.0	-0.51	0.65	-0.42	-0.0	0.0	0.0	0.0	0.70	-0.03	-0.63	0.68	0.02				
1.75	0.0009	0.65	0.67	0.0	0.62	0.50	-0.48	0.0	-0.69	0.44	-0.42	-0.0	0.0	0.0	0.0	0.51	0.23	-0.59	0.64	0.21				
1.78	-0.08	0.72	0.59	0.0	0.50	0.53	-0.58	-0.0	-0.78	0.26	-0.43	-0.0	0.0	0.0	0.0	0.51	0.38	-0.53	0.56	0.34				
1.81	-0.20	0.76	0.50	0.0	0.40	0.53	-0.64	-0.0	-0.81	0.08	-0.44	-0.0	0.0	0.0	0.0	0.66	0.49	-0.44	0.47	0.45				
1.83	-0.27	0.77	0.46	0.0	0.36	0.53	-0.67	-0.0	-0.81	-0.014	-0.45	-0.0	0.0	0.0	0.0	0.70	0.54	-0.38	0.41	0.50				
1.85	-0.33	0.77	0.42	0.0	0.34	0.53	-0.70	-0.0	-0.80	-0.09	-0.46	-0.0	0.0	0.0	0.0	0.75	0.58	-0.33	0.36	0.54				
1.90	-0.43	0.76	0.34	0.0	0.31	0.50	-0.71	-0.0	-0.76	-0.21	-0.48	-0.0	0.0	0.0	0.0	0.81	0.63	-0.24	0.26	0.58				
2.00	-0.52	0.73	0.26	0.0	0.35	0.49	-0.70	-0.0	-0.68	-0.29	-0.55	-0.0	0.0	0.0	0.0	0.87	0.67	-0.15	0.17	0.61				
2.10	-0.55	0.72	0.21	0.0	0.42	0.51	-0.65	0.0	-0.62	-0.28	-0.62	-0.0	0.0	0.0	0.0	0.88	0.68	-0.11	0.14	0.62				
2.20	-0.56	0.73	0.19	0.0	0.49	0.52	-0.58	0.0	-0.56	-0.24	-0.69	-0.0	0.0	0.0	0.0	0.89	0.68	-0.10	0.13	0.62				
2.30	-0.56	0.73	0.17	0.0	0.55	0.53	-0.51	0.0	-0.49	-0.20	-0.75	-0.0	0.0	0.0	0.0	0.89	0.69	-0.10	0.14	0.62				
2.35	-0.55	0.74	0.16	0.0	0.58	0.53	-0.47	0.09	-0.46	-0.17	-0.78	-0.0	0.0	0.0	0.0	0.89	0.69	-0.10	0.14	0.62				
2.50	-0.52	0.76	0.15	0.0	0.65	0.52	-0.38	0.13	-0.39	-0.10	-0.83	-0.0	0.0	0.0	0.0	0.89	0.69	-0.11	0.16	0.6				
2.65	0.01	0.93	0.10	0.0	0.87	0.01	-0.28	0.17	-0.26	0.02	-0.34	0.80	0.17	-0.10	0.78	0.40	0.58	-0.44	0.52	0.43				
2.70	0.02	0.93	0.10	0.0	0.87	0.005	-0.26	0.18	-0.20	-0.01	-0.05	0.89	0.24	-0.10	0.85	0.10	0.48	-0.44	0.52	0.43				
3.00	0.03	0.93	0.08	0.0	0.87	0.02	-0.21	0.25	-0.26	-0.01	-0.004	0.88	0.19	-0.10	0.87	0.07	0.48	-0.44	0.53	0.42				
3.50	0.05	0.93	0.08	-0.0	0.86	-0.05	-0.17	0.32	-0.32	-0.01	0.005	0.85	0.15	-0.09	0.88	0.04	0.48	-0.44	0.53	0.42				
5.00	0.07	0.93	0.07	0.0	0.84	-0.07	-0.15	0.35	-0.35	-0.01	0.006	0.84	0.13	-0.09	0.88	0.04	0.48	-0.44	0.54	0.43				
50.0	0.07	0.93	0.07	0.0	0.84	-0.07	-0.15	0.35	-0.35	-0.01	0.005	0.84	0.12	-0.09	0.88	0.04	0.48	-0.44	0.54	0.43				

q_a/ Å	$C_{\alpha,1}$	$C_{\alpha,2}$	$C_{\alpha,3}$	$C_{\alpha,4}$	$C_{\alpha,5}$	$C_{\alpha,6}$	$C_{\beta,1}$	$C_{\beta,2}$	$C_{\beta,3}$	$C_{\beta,4}$	$C_{\beta,5}$	$C_{\beta,6}$	$C_{\gamma,1}$	$C_{\gamma,2}$	$C_{\gamma,3}$	$C_{\gamma,4}$	$C_{\gamma,5}$	$C_{\gamma,6}$	$C_{\delta,1}$	$C_{\delta,2}$	$C_{\delta,3}$	$C_{\delta,4}$	$C_{\delta,5}$	$C_{\delta,6}$
1.20	0.00	0.95	0.00	0.00	0.00	0.00	0.52	0.00	0.00	0.77	0.00	0.00	0.77	0.00	0.00	-0.52	0.00	0.00	-	not	con-	ver-	ged	-
1.50	0.27	0.89	0.00	0.00	0.00	0.00	0.67	-0.16	0.00	0.63	0.00	0.00	-0.59	0.24	0.00	0.69	0.00	0.00	0.00	0.00	0.87	0.00	0.00	0.00
1.60	0.46	0.81	0.00	-0.12	0.00	0.00	0.58	-0.23	0.00	0.70	0.00	0.00	-0.57	0.41	0.00	0.61	0.00	0.00	0.00	0.00	0.88	0.00	0.00	0.00
1.70	0.26	0.89	0.00	-0.18	0.00	0.00	0.55	0.00	0.22	0.73	0.00	0.00	0.71	-0.31	0.00	-0.51	0.00	0.00	0.00	0.00	0.90	-0.22	0.00	0.00
1.75	0.25	0.84	-0.10	-0.31	0.00	0.00	0.57	0.12	0.29	0.68	0.00	0.00	0.70	-0.39	-0.06	-0.48	0.00	0.00	-0.10	0.00	0.87	-0.28	0.00	0.00
1.81	-0.19	0.48	-0.65	-0.45	0.00	0.00	0.57	0.69	0.19	0.21	0.00	0.00	0.70	-0.41	-0.44	0.00	0.00	0.00	-0.16	0.00	-0.45	0.79	0.00	0.00
1.83	-0.25	0.36	-0.56	-0.61	0.00	0.00	0.54	0.76	0.10	0.14	0.00	0.00	0.71	-0.42	-0.42	-0.13	0.00	0.00	0.16	0.00	0.55	-0.72	0.00	0.00
1.85	-0.29	0.30	-0.51	-0.67	0.00	0.00	0.52	0.78	0.00	0.10	0.00	0.00	0.71	-0.42	-0.38	-0.19	0.00	0.00	0.16	0.00	0.66	-0.62	0.00	0.00
1.90	-0.30	0.22	-0.25	-0.83	0.00	0.00	0.48	0.81	0.00	0.00	0.00	0.00	0.73	-0.42	-0.30	-0.28	0.00	0.00	0.18	0.00	0.84	-0.34	0.00	0.00
2.30	-0.24	0.00	0.00	-0.90	0.00	0.00	0.24	0.90	0.00	0.00	0.00	0.00	0.86	-0.22	0.00	-0.24	0.00	0.00	-0.06	0.00	-0.88	0.00	0.08	0.00
2.50	-0.21	0.00	0.00	-0.89	0.00	0.00	0.24	0.90	0.00	0.00	0.00	0.00	0.86	-0.23	0.00	-0.22	0.00	0.00	0.00	0.00	0.70	0.00	0.52	-0.31
2.70	-0.20	0.00	0.00	-0.92	0.00	0.00	-0.17	0.76	0.00	0.00	-0.52	0.00	0.00	0.53	0.00	0.00	0.70	0.00	0.89	0.16	0.00	-0.19	0.00	0.00
3.00	-0.18	0.00	0.00	-0.92	0.00	0.00	0.00	0.00	0.00	0.00	0.93	0.00	-0.19	0.91	0.00	0.00	0.00	0.00	0.88	0.19	0.00	-0.17	0.00	0.09
3.50	-0.15	0.00	0.00	-0.93	0.00	0.00	0.00	0.00	0.00	0.00	0.87	-0.34	0.12	0.90	0.00	0.00	0.00	0.21	0.00	-0.23	0.00	0.00	0.33	0.83
5.00	-0.15	0.00	0.00	-0.93	0.00	0.00	0.00	0.00	0.00	0.00	0.88	-0.29	0.08	0.55	0.00	0.00	0.23	0.71	0.00	0.75	0.00	0.00	0.00	-0.52
50.0	0.15	0.00	0.00	-0.93	0.00	0.00	0.00	0.00	0.00	0.00	0.89	0.29	0.00	0.48	0.00	0.00	-0.24	0.74	0.00	0.80	0.00	0.00	0.00	-0.45

3.7 Ionic potentials and approximated transition dipole moments between ionic and neutral states

3.7.1 Ionic state potentials

To simulate pump-probe ionization spectra the low-lying ionic states have been calculated at the same level of theory as the neutral electronic states. During the ionization process one electron is removed from the neutral molecule:

$$\mathrm{CpMn(CO)_3} \overset{h\nu}{\rightarrow} \mathrm{CpMnCO_3^+} + \mathrm{e^-}.$$

The detached electron moves as a free particle described by a plane wave. Like the neutral state, the ion can be described by a CI expansion:

$$|\Phi_i^{ion}(q_a)\rangle = \sum_j C_{ij}^{ion}(q_a)|D_j^{ion}(q_a)\rangle, \tag{3.3}$$

where the $|D_j^{ion}(\underline{q_a})\rangle$ are the state configurations representing the ionic state. Removing one electron from CpMn(CO)$_3$ leads to doublet ionic states. The three energetically lowest ones, calculated by CASSCF/MR-CCI, are the here so called a^2A'', a^2A' and b^2A' states, as depicted in figure 3.13. They are bound states showing no crossing between the Frank-Condon point and the asymptotic region. Our calculations show that the next higher doublet states are separated from these three lowest states by approximately 1 eV. All three states are described by one dominant configuration (*cf* expansion (3.3)) which differs from the ground state by removing one electron from the d_{xy}, the $d_{x^2-y^2}$ and the d_{z^2} orbital, respectively:

$$a^2A'' : (d_{z^2})^2, (d_{x^2-y^2})^2, (d_{xy})^1$$

$$a^2A' : (d_{z^2})^2, (d_{x^2-y^2})^1, (d_{xy})^2$$

$$b^2A' : (d_{z^2})^1, (d_{x^2-y^2})^2, (d_{xy})^2$$

The resulting configurations are depicted in figure 3.14.

3.7.2 Transition dipole moments between the neutral A' states and the ionic states

The free electron removed from the neutral molecule has a continuous spectrum of momentum eigenvalues. No selection rules for transitions from the excited to

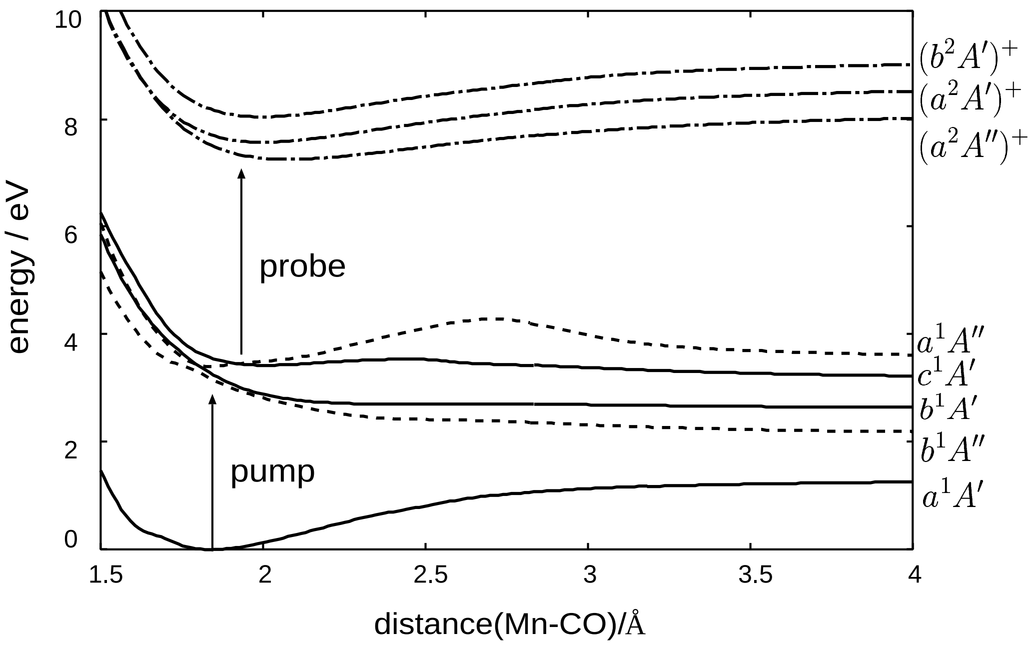

Figure 3.13: *The three lowest singlet cationic states, with the four lowest singlet excited states and the electronic ground state of CpMnCO$_3$, all calculated at CASSCF/MR-CCI level of theory.*

the ionic states can be applied. Nevertheless a one-photon transition from the excited neutral state to an ionic state costs less energy than for example a multiphoton transition directly from the neutral ground or via several excited states to the same ionic state and should be more probable. Therefore, in the pump probe (excitation-ionization) process the the molecular orbital from which the electron is removed to get a specific ionic state configurations should correspond to the excitation in the neutral excited state.

The transition dipole moment is written as the electric dipole operator sandwiched between the ionic and the neutral state:

$$TDM^{x/y/z}_{neutral \rightarrow ion} = \langle \Phi_i^{ion} | \mu_{ij,x/y/z} | \Phi_j \rangle = \sum_k C_{jk} \langle D_i^{ion}(\underline{q_a}) | \mu_{ij,x/y/z} | D_k \rangle, \quad (3.4)$$

where the ionic state is described by one configuration, $\Phi_i^{ion} = D_i^{ion}$, and the neutral state consists of a linear combination of several configurations, $|\Phi_j\rangle = \sum C_{jk}|D_k\rangle$. Since μ is a 1-particle operator, the Condon-Slater rules impose that if the neutral state configuration D_k differs from an ionic configuration in more than one molecular orbital the corresponding matrix element vanishes. For instance, for $\Phi_i^{ion} = (a^2A'')^+$ and $|\Phi_j\rangle = b^1A'$ one obtains:

$$\text{transition dipole: } b^1A' \rightarrow (a^2A'')^+ \propto C_{b,3}$$

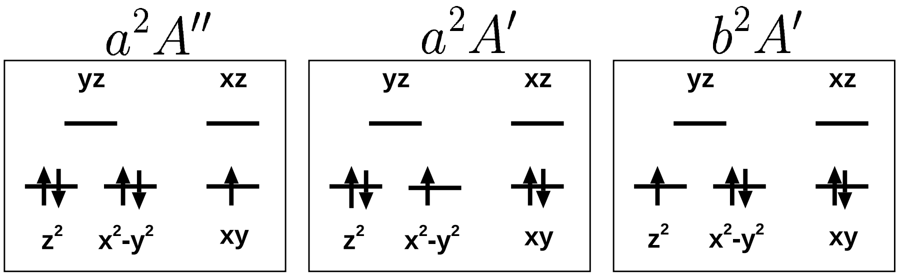

Figure 3.14: *Principal configuration of the ionic states a^2A'', a^2A' and b^2A'. Compared with the ground state configuration one electron is removed from the d_{xy}, the $d_{x^2-y^2}$ and the d_{z^2} orbital, respectively.*

since the ionic configuration a^2A'' (figure 3.14) differs from the configuration D_3 (figure 3.5) in only one orbital, but in more than one orbital from D_1, D_2 and D_4. In an analogous way the transition dipole between the c^1A' neutral and $(a^2A'')^+$ ionic state can be approximated by:

$$\text{transition dipole: } c^1A' \rightarrow (a^2A'')^+ \propto C_{c,3}$$

To find the dipole moments between the b and c excited state and the other two ionic states the mixing between the $d_{x^2-y^2}$ and the d_{z^2} character present in the orbitals $21a'$ and $22a'$ has to be taken into account. The contribution of the $d_{x^2-y^2} \rightarrow d_{yz}$ excitation which is preferable if the a^2A' is to be created can be calculated using the CI coefficients and the orbital coefficients of the b and c state as follows:

$$\text{transition dipole: } b^1A' \rightarrow (a^2A')^+ \propto C_{b,1} \cdot k_{21,x^2-y^2} + C_{b,2} \cdot k_{22,x^2-y^2}$$

$$\text{transition dipole: } c^1A' \rightarrow (a^2A')^+ \propto C_{c,1} \cdot k_{21,x^2-y^2} + C_{c,2} \cdot k_{22,x^2-y^2}$$

The corresponding calculation to get the $d_{z^2} \rightarrow d_{yz}$ contribution which leads to the cation b^2A' state is:

$$\text{transition dipole: } b^1A' \rightarrow (b^2A')^+ \propto C_{b,1} \cdot k_{21,z^2} + C_{b,2} \cdot k_{22,z^2}$$

$$\text{transition dipole: } c^1A' \rightarrow (b^2A')^+ \propto C_{c,1} \cdot k_{21,z^2} + C_{c,2} \cdot k_{22,z^2}$$

With these considerations, the resulting transition dipole moments for the b^1A' and c^1A' states are plotted in figures 3.15 and 3.16 respectively.

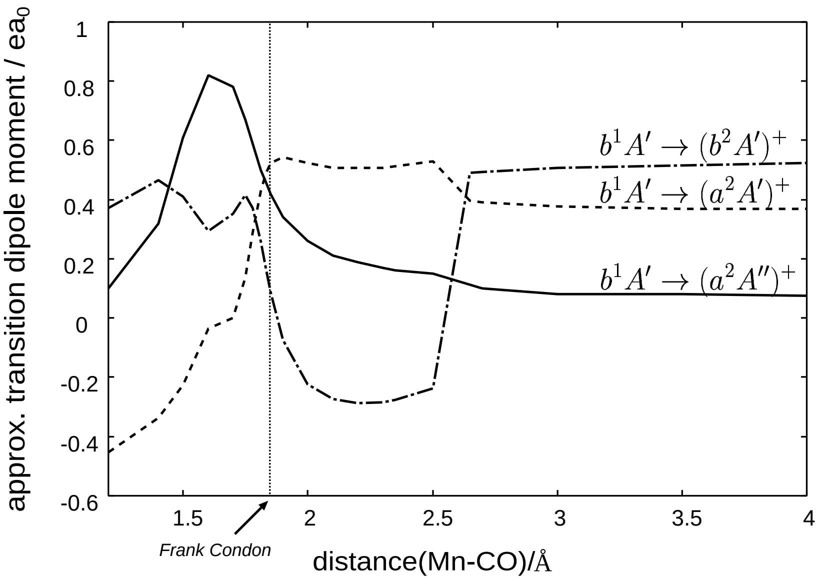

Figure 3.15: *Electronic transition dipole moments connecting the excited state* b^1A' *with the cationic states* a^2A'' *(solid line),* a^2A' *(dashed line) and* b^2A' *(dot-dashed line) approximated using the CI- and orbital-coefficients (see text).*

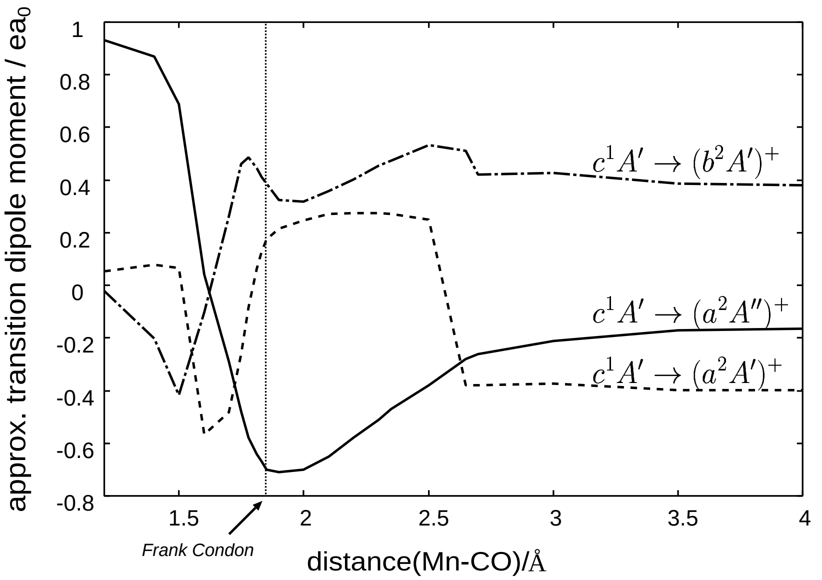

Figure 3.16: *Electronic transition dipole moments connecting the excited state* c^1A' *with the cationic states* a^2A'' *(solid line),* a^2A' *(dashed line) and* b^2A' *(dot-dashed line) approximated using the CI- and orbital-coefficients (see text).*

3.7.3 Transition dipole moments coupling the A'' states with the ionic states

In the A'' case a strong orbital mixing between the d_{z^2} and the $d_{x^2-y^2}$ orbitals does not appear. Using the same reasoning as for the A' states the transition dipole moments can be approximated by the CI coefficients of table 3.6 The comparison of the configurations of the a^1A'' and b^1A'' states (figure 3.9) with the configurations of the ionic states (figure 3.14) determines which CI coefficients serve to approximate the transition dipole moments.

$$\text{transition dipole: } a^1A'' \rightarrow (a^2A'')^+ \propto C_{\alpha,3} + C_{\alpha,4}$$

$$\text{transition dipole: } b^1A'' \rightarrow (a^2A'')^+ \propto C_{\beta,3} + C_{\beta,4}$$

$$\text{transition dipole: } a^1A'' \rightarrow (a^2A')^+ \propto C_{\alpha,2}$$

$$\text{transition dipole: } b^1A'' \rightarrow (a^2A')^+ \propto C_{\beta,2}$$

$$\text{transition dipole: } a^1A'' \rightarrow (b^2A')^+ \propto C_{\alpha,1}$$

$$\text{transition dipole: } b^1A'' \rightarrow (b^2A')^+ \propto C_{\beta,1}$$

The resulting transition dipole moments for the b^1A' and c^1A' states are plotted in figures 3.17 and 3.18 respectively.

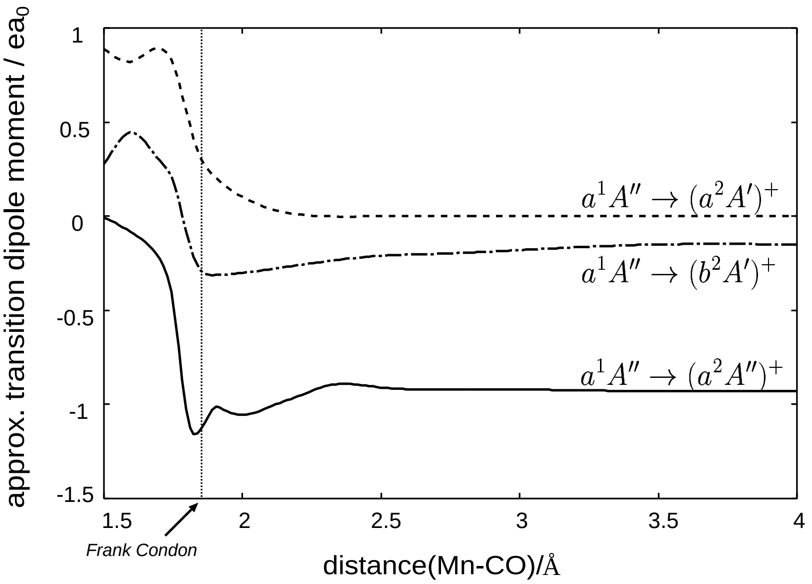

Figure 3.17: *Electronic transition dipole moments connecting the excited state* c^1A' *with the cationic states* a^2A'' *(solid line),* a^2A' *(dashed line) and* b^2A' *(dot-dashed line) approximated using the CI- and orbital-coefficients (see text).*

Note that the presented TDM for $neutral \to ionic$ transitions are only proportional (”$\propto$”) to the CI coefficients. Therefore, only the relative and not the absolute values of these TDM are known and the pump-probe spectra in chapter 4 are represented by the population of the ionic states only in ”arbitrary” units.

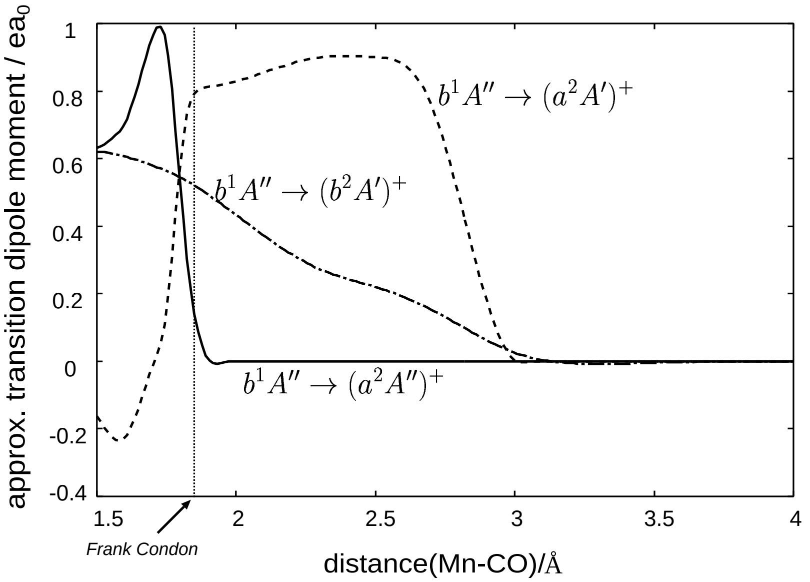

Figure 3.18: *Electronic transition dipole moments connecting the excited state* c^1A' *with the cationic states* a^2A'' *(solid line),* a^2A' *(dashed line) and* b^2A' *(dot-dashed line) approximated using the CI- and orbital-coefficients (see text).*